RSC Advances

PAPER

View Article Online
View Journal | View Issue

Cite this: *RSC Adv.*, 2019, **9**, 16130

High proton conductivity behavior in a 2D metal sulfite constructed from a histidine ligand†

Yike Ma,[a] Liangliang Huang,*[a] Zhijia Xiu,[a] Yuheng Yang,[a] Xiaodong Wang,[a] Yanzhen Yin,*[c] Yanfeng Bi*[a] and Zhiping Zheng[ab]

Received 2nd March 2019
Accepted 22nd April 2019

DOI: 10.1039/c9ra01584a

rsc.li/rsc-advances

In the presence of the amino acid histidine, an inorganic–organic hybrid metal sulfite, $Zn_2(SO_3)_2(C_6N_3O_2H_9)_2 \cdot H_2O$ (**1**), has been prepared under hydrothermal conditions. Single-crystal X-ray diffraction analysis reveals that **1** shows a 2D layer framework built up from a classical second building unit (S4R), and bridged histidine molecule. Notably, it is the first report of a metal sulfite in the presence of an amino acid molecule. A 1D H-bonding array can be constructed by the H-bonding interaction between histidine molecules and sulfite groups. Moreover, a new function of metal sulfite for proton conduction was investigated by alternating-current impedance analysis. The results demonstrate that compound **1** shows a high proton conductivity of approximately 10^{-3} S cm^{-1} at 348 K and 98% relative humidity.

Introduction

Proton-conducting materials have received extensive attention because of their applications in a variety of electrical and electrochemical devices, especially in fuel cells.[1–4] Nafion is one of the most important popular materials that is being used as an electrolyte membrane with a high proton conductivity of 10^{-2} S cm^{-1} at 60–80 °C under 98% relative humidity (RH).[5] However, this material suffers from several limitations, such as high cost, limited operating temperature and the difficulty of optimizing the proton transport pathway.[6] Therefore, it is necessary to design and synthesize new materials which maintain high proton conductivity with low cost and a wide operating temperature.

Crystalline porous materials, with framework diversity, tunability and porosity, have become ideal candidates for proton-conducting applications. In addition, they provide theoretical guidance for the synthesis of new proton-conducting materials because the crystalline nature of crystalline porous materials provides an opportunity to study the proton-conduction pathway and mechanism.[7–11] Inorganic open-framework materials based on oxyanions, such as phosphates,[12,13] phosphites,[14–16] and sulfates,[17,18] exhibit well-defined pore architectures and variable framework compositions. On the one hand, proton carriers (*e.g.*, H_3O^+, NH_4^+, imidazole, H_2O and –COOH) can be easily introduced into their free voids or in their frameworks, which is an effective approach to prepare high performance proton-conducting materials.[19–22] On the other hand, the hydrogen bond networks between host–guest or guest–guest can provide proton-conducting pathways.[23–27] In addition, high hydrothermal stability which is very important for proton-conducting materials in fuel cells is usually another significant feature of these materials.[24,28] Current endeavors on the study of proton-conducting materials have demonstrated that metal phosphates, phosphites and sulfates show proton conduction.[29–35] For example, $[\{In_2(\mu\text{-}OH)_2(SO_4)_4\}\cdot\{(LH)_4\}\cdot nH_2O]_n$ (LH = protonated melamine) carries a continuous water array functioning as a solid-state proton conductor ($\sigma = 4.4 \times 10^{-5}$ S cm^{-1}, 98% RH, and $T = 303.15$ K), a three-dimensional beryllium phosphate with intersecting 24-membered ring channels displays exceptional hydrothermal stability and shows a high proton conductivity on the order of 10^{-3} S cm^{-1} at 25 °C under high humidity conditions.[34,35]

We are particularly interested in the use of 3-connected centers as basic structural units for the construction of inorganic open-framework materials, such as a chiral indium phosphite with intertwined host and guest helices and a layered cobalt phosphite-oxalate with proton conductivity.[36,37] In order to expand the field of research concerning inorganic open-framework materials with 3-connected centers as basic structural units, we try to introduce sulfite into the inorganic framework. However, because of the instability of S in its +4 oxidation state, sulfates are usually obtained as products in

[a]*School of Chemistry and Material Science, Liaoning Shihua University, Fushun 113001, Liaoning, P. R. China. E-mail: huangll@lnpu.edu.cn; biyanfeng@lnpu.edu.cn*
[b]*Shenzhen Grubbs Institute, Department of Chemistry, Southern University of Science and Technology, Shenzhen, Guangdong, 518000, P. R. China*
[c]*Qinzhou Key Laboratory of Biowaste Resources for Selenium-Enriched Functional Utilization, College of Petroleum and Chemical Engineering, Beibu Gulf University, Qinzhou, 535011, Guangxi, P. R. China. E-mail: yinyanzhen2018@163.com*

† Electronic supplementary information (ESI) available: The crystallographic information files (CIF); bond lengths and angles, and hydrogen bonds. XRD, TGA, IR spectrum, photoluminescence spectrum, asymmetric unit structure, 1D H-bonding array, and Nyquist plots at various temperatures under 44% RH, 58% RH and 76% RH. CCDC 1892957. For ESI and crystallographic data in CIF or other electronic format see DOI: 10.1039/c9ra01584a

most of the reactions even when SO_3^{2-} is used as the S source. Probably due to this difficulty, there are few open-framework metal sulfites known.[38–40] Herein, we use histidine as the organic template to synthesize a metal sulfite. Histidine molecules have a variety of coordination modes, and each functional group can be bonded to a metal center, wherein carboxylic acid is often introduced as a functional group capable of improving proton conduction properties in a proton conductive material, and a side chain imidazole is a common ligand in metal inorganic–organic hybrid materials, these functional groups can enhance proton conduction efficiency in theory.[8–11]

In this paper, a 2D layered zinc sulfite $Zn_2(SO_3)_2(C_6N_3O_2H_9)_2\cdot H_2O$ with a histidine molecule as the ligand has been hydrothermally synthesized, which is the first report of a metal sulfite in the presence of an amino acid molecule. Notably, this compound shows a high proton conductivity in the order of 10^{-3} S cm^{-1} at 348 K and 98% RH.

Experimental section

Materials and instrumentation

All chemical samples were obtained from commercial sources and used without further purification. The X-ray diffraction (XRD) pattern was obtained with a Bruker D8 Advance diffractometer with Cu-Kα ($\lambda = 1.5418$ Å, 40 kV, 40 mA) radiation in the scan range of 4–40° with a step size of 0.02°. The elemental analysis was conducted on a Vario EL cube elemental analyzer. ICP-AES (inductively coupled plasma-atomic emission spectroscope) analysis was performed on a PerkinElmer Optima 3300DV ICP instrument. FT-IR spectra was recorded on a Nicolet Impact 410 spectrometer between 400 and 4000 cm^{-1} using the KBr pellet method. Thermogravimetric analysis (TGA) was conducted on a PerkinElmer TGA 7 thermogravimetric analyzer at a ramp rate of 10 °C min^{-1} under a flow of air gas from room temperature to 800 °C. Photoluminescence analyses were performed on an Edinburgh Instrument FLS920 luminescence spectrometer.

Synthesis

The zinc sulfite compound, $Zn_2(SO_3)_2(C_6N_3O_2H_9)_2\cdot H_2O$, was synthesized from $Zn(Ac)_2\cdot 4H_2O$, $NaHSO_3$, and L-histidine in a H_2O solution. A mixture of 0.1 g $Zn(Ac)_2\cdot 4H_2O$, 0.4 g sodium hydrogen sulfite ($NaHSO_3$), and 0.2 g L-histidine was dissolved in 2.0 mL of water. The mixture was further stirred for 30 minutes at room temperature and heated at 115 °C for 5 days in a 23 ml Teflon-lined stainless steel autoclave (filled up to 27% volume capacity), followed by slow cooling down to the ambient temperature. Colorless crystals could be achieved, washed with water, then filtered, and dried in air. The yield of the product was 56% in weight based on zinc. The experimental XRD pattern are in good agreement with the simulated ones from the single-crystal X-ray diffraction (Fig. S1†). Analysis found (wt%): Zn, 21.07; S, 10.25; C, 23.16; H, 3.18; N, 13.65; calcd (wt%): Zn, 21.12; S, 10.36; C, 23.27; H, 3.26; N, 13.57. IR data (KBr, cm^{-1}): 3133 m, 3037 m, 2910 m, 1644 s, 1585 s, 1409 m, 1367 w, 1292 w, 1267 w, 1230 w, 1145 w, 1101 w, 1037 w, 937 s, 900 m, 838 w, 817 w, 784 w, 721 w, 692 m, 632 m, 547 w, 507 m, 440 w.

Determination of crystal structure

A suitable single crystal with dimensions of 0.20 × 0.21 × 0.22 mm^3 of compound **1** was carefully selected under an optical microscope for single crystal XRD analysis. Single-crystal structure determination by X-ray diffraction was performed on a Bruker D8 Quest diffractometer with graphite-monochromated Mo-Kα ($\lambda = 0.71073$ Å) radiation at a temperature of 296 K. Data processing was accomplished with the saint-processing program. The structure was solved by a direct method using the SHELXTL-2014 crystallographic software package.[41,42] The zinc and sulphur atoms were first located, whereas the carbon, nitrogen and oxygen atoms were found in the different Fourier maps. All the hydrogen atoms were placed geometrically and refined in a riding model. All of the non-hydrogen atoms were refined anisotropically.

The detailed crystallographic data and selected bond lengths as well as the bond angles for compound **1** are listed in Table 1 and S1.† CCDC-1892957 contains the supplementary crystallographic data for this paper.

Proton conductivity measurement

The hydrated proton conductivities of the compound pellets were measured using a CHI660E electrochemical work station. The alternating current frequencies ranged from 1 Hz to 10^6 Hz. Variable impedance spectra were collected at different humidity and temperatures. The humidity was controlled by different saturated aqueous salt solutions, which were salt solutions of Na_2HPO_4 (98% RH), NaCl (76% RH), NaBr (58% RH) and K_2CO_3 (44% RH). The conductivity measurement was performed after setting the sample at different humidities for approximately 48 hours. The proton conductivity (S cm^{-1}) was calculated using the formula $\sigma = L/AR$, where L is the pellet thickness, A is the pellet area (7 mm in diameter and 0.8 mm in thickness), and R is the compound impedance obtained from the Nyquist plot.

Table 1 Crystal data and structure refinement for compound **1**

Empirical formula	$C_{12}H_{20}N_6O_{11}S_2Zn_2$
Formula weight	619.26
Temperature/K	296(2)
Crystal system	Monoclinic
Space group	*C*2/*c*
a/Å	14.6764(7)
b/Å	8.3407(4)
c/Å	16.8021(8)
β/°	101.397(2)
V/Å^3	2016.21(17)
Z	4
Calculated density/g cm^{-3}	2.040
Absorption coefficient/mm^{-1}	2.660
F(000)	1256
Theta range for data collection/°	2.5 to 25.1
Refinement method/unique	8485/1782 [*R*(int) = 0.034]
Refinement method	Full-matrix least-squares on F^2
Data/restraints/parameters	1782/0/151
Goodness-of-fit on F^2	1.05
Final *R* indices [*I* > 2 sigma(*I*)]	$R_1 = 0.0258$, w$R_2 = 0.0574$
R indices (all data)	$R_1 = 0.0350$, w$R_2 = 0.0608$
Largest diff. peak and hole/(e Å^{-3})	0.32 and −0.28

The E_a value was derived from the Arrhenius equation: $T\sigma = \sigma_0 \exp(-E_a/kT)$, where σ_0 is a pre-exponential factor, E_a is the activation energy, and k is the Boltzmann constant.

Results and discussion

Structural description

The single crystal X-ray analysis reveals that **1** crystallizes in the monoclinic crystal system with the *C*2/*c* space group. The asymmetric unit contains one Zn atom, one S atom, one L-histidine cation and one free lattice water molecule (Fig. S3†). The crystallographically independent Zn atom is tetrahedrally coordinated to two O atoms bridging to the neighboring S atoms, one carboxyl O atom and one N atom from the imidazole of the L-histidine cations. The Zn–O bond lengths are in the range of 1.9247(18)–1.9853(19) Å and the O–Zn–O bond angles vary in the range of 102.49(8)–112.68(8)°. The Zn–N bond length is 1.989(2) Å. The crystallographically independent S atom is three-coordinated to oxygen atoms and shares two oxygen atoms with adjacent Zn atoms, with the third trigonal pyramidal vertex occupied by an terminal oxygen atom [d (S=O) = 1.5167(18) Å]. The S–O bridging bond lengths are in the range of 1.5167(18)–1.5362(19) Å and the average O–S–O bond angle is 104.83°.

As shown in Fig. 1a, the framework of $Zn_2(SO_3)_2(C_6N_3O_2H_9)_2 \cdot H_2O$ shows a 2D layered structure, which is built up from a second building unit, namely a single four-membered ring (S4R) and a histidine molecule. The S4R, $(ZnSO_3)_2$, is formed from two tetrahedral Zn^{2+} cations and two SO_3^{2-} sulfite anions. The histidine molecule is neutral zwitterionic and serves as a bidentate ligand connecting with the adjacent two S4Rs to form a 2D inorganic–organic hybrid layer. In the layer, six Zn(II) ions, two sulfites and four histidine molecules get together and form a 12-membered ring window.

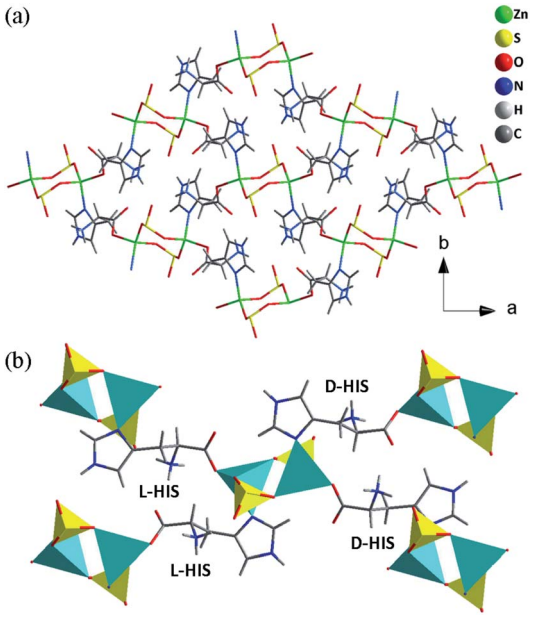

Fig. 1 The structure of compound **1**: (a) the 2D layer with the 12-membered ring window. (b) The connection between histidine molecules and S4Rs (HIS: histidine).

As shown in Fig. 1b, each S4R is surrounded by two pairs of histidine molecules while each histidine molecule is connected with the adjacent two S4Rs. It is noteworthy that the histidine molecules surrounding the S4R show two different absolute configurations. A pair of histidine molecules on one side of the S4R has the *R* absolute configuration while the other pair of those on the other side of the S4R has the *S* absolute configuration. As a result, compound **1** is achiral, although the initially added histidine is homochiral. It is demonstrated that the racemization happened in the hydrothermal synthetic system. A similar phenomenon was observed in the synthesis of $Zn(HPO_4)(C_6H_9N_3O_2)$, $Zn(HPO_3)(DL\text{-}C_6H_9N_3O_2)(H_2O)_{0.5}$ and ZnPO-CJ36.[43–45] In order to contrast experiment results, we used D,L-histidine and D-histidine to replace the L-histidine in the system of reaction, but the final structure is not charged and it is still compound **1**. The result further demonstrated that a single chiral histidine does not easily exist in the final structure under hydrothermal synthesis.

As shown in Fig. 2, the 2D layers are stacked in an ABAB sequence along the *a* axis. The lattice water molecules are situated in between the layers, which are held *via* extensive O(W)–H···O hydrogen bonding interactions between guest molecules and the host framework. The O···O distance is 2.83 Å. The H bond provides extra stability to the lattice water molecules, which has been confirmed by the TGA of the powder sample of compound **1** showing a continuous initial loss.[34] Extensive hydrogen bonds are also formed between the histidine molecules and sulfite units. The $N(2)H_3^-$ group forms three hydrogen bonds to one terminal C=O group ($d_{N\cdots O}$ = 2.848(3) Å), two terminal oxygen atoms from sulfite units with an average N···O distance of 2.82 Å. The $N(3)H^-$ groups of the imidazole moiety form one hydrogen bond with the terminal O(3) atom from the sulfite unit with a distance of 2.791(3) Å. In addition, there are three types of weak C–H···O hydrogen-bonding interactions: the interaction between the chiral tertiary carbon C(2) atom and the μ_2-O(4) of the carboxyl oxygen atoms, the interaction between the C(5) atom from imidazole and the terminal O(5) of the carboxyl oxygen atoms, and the interaction between the C(6) atom from imidazole and μ_2-O(2) of the sulfite group. Because of the H-bond interactions between the histidine molecules and sulfite groups, a 1D H-bonding array can be constructed (Fig. S4†). Finally, the hydrogen bonding interactions among water molecules, histidine molecules and sulfite

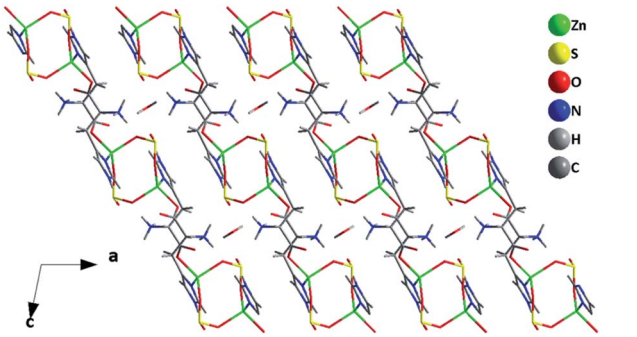

Fig. 2 The 2D layers are stacked in an ABAB sequence along the *a* axis.

units construct a pseudo-3D supramolecular structure (Fig. 3). The detailed H-bond data is listed in Table S2.†

As far as we know, compound **1** is the first zinc sulfite to be prepared in the presence of a histidine molecule. The histidine acts as a bridge between inorganic secondary building blocks which directly cross-link to the framework. In the past, although some zinc sulfite frameworks are already reported such as $(NH_3CH_2CH_2NH_3)[Zn_3(SO_3)_4]$,[40] the structure of cross-linking organic metal-sulfites has been rarely reported.

Proton conductivity

In the structure of $Zn_2(SO_3)_2(C_6N_3O_2H_9)\cdot H_2O$, there are water molecules and a 1D H-bonding array. Therefore, compound **1** is expected to conduct protons and proton conduction behavior was investigated by AC impedance measurement both as a function of temperature at constant RH and as a function of RH at constant temperature. The proton conductivity was estimated from the Nyquist plots shown in Fig. 4, 5 and S5–S7.† The proton conductivity of different relative humidity (RH) at 303 K was measured. It was demonstrated that the proton conductivity increases with the increase of humidity (Fig. 4). This phenomenon is well proven at low temperatures, the proton conductivity is 2.05×10^{-9} S cm^{-1} under 44% RH and reaches 1.01×10^{-5} S cm^{-1} under 98% RH. Even though the proton conductivity of **1** was not remarkable at room temperature and 98% RH, it is comparable to several materials such as $[Zn(D\text{-}LCl)(Cl)](H_2O)_2$ (4.42×10^{-5} S cm^{-1} at 304 K, 98% RH), $[H_3O][Ni(SO_4)F]$ (7.9×10^{-6} S cm^{-1} at 298 K, 98% RH) and

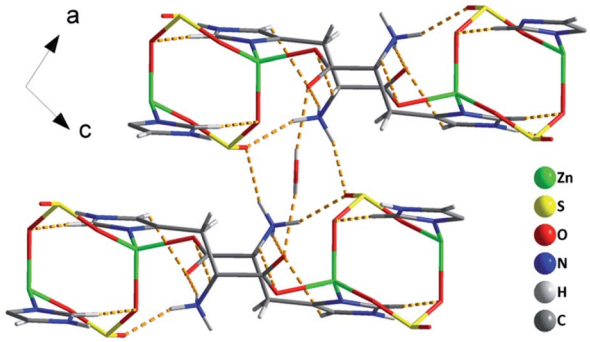

Fig. 3 View of H-bonding interactions existing in the structure of **1**.

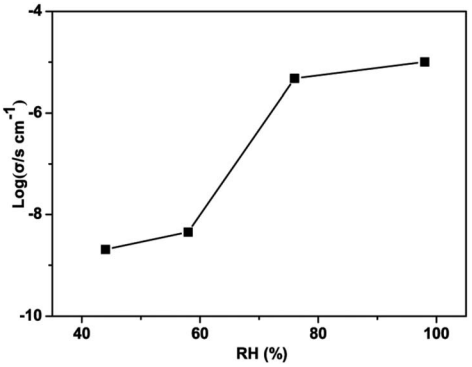

Fig. 4 Humidity dependence of the proton conductivity at 303 K.

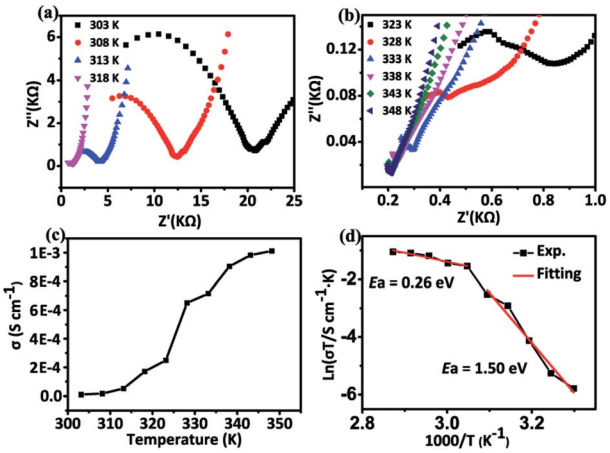

Fig. 5 (a) and (b) Nyquist plots of **1** at various temperatures under 98% RH. (c) Temperature dependence of the proton conductivity of **1**. (d) Arrhenius plot of **1**.

$[\{In_2(OH)_2(SO_4)_4\}\cdot\{(LH)_4\}\cdot nH_2O]_n$ (4.4×10^{-5} S cm^{-1} at 303 K, 98% RH).[34,46] As shown in Fig. S5–S7,† we found that at high temperature under humid conditions, the semicircle of the Nyquist plot basically disappears, which is similar to the phenomenon reported previously in the literature.[47–49]

To gain insight into the proton-conduction mechanism, we calculated the activation energy at different temperatures under 98% RH (Fig. 5). It is obvious that the resistance of the compound decreases with increasing temperature, indicating a sustained increase in proton conductivity. The proton conductivity increased from 1.01×10^{-5} S cm^{-1} at 303 K to 2.49×10^{-4} S cm^{-1} at 323 K. It is worth noting that the conductivity has a jump in growth around 323 K, and a maximum value is reached 1.01×10^{-3} S cm^{-1} at 348 K. This value was comparable to some MOFs such as $[LnL(H_2O)_3]\cdot 2H_2O$ (L = *N*-phenyl-*N*′-phenylbicyclo-[2,2,2]-oct-7-ene-2,3,5,6-tetra-carboxdiimide tetracarboxylic acid, Ln = Eu, Dy) (10^{-5} S cm^{-1}, 343 K, 97% RH), POMs such as NENU-530 (10^{-3} S cm^{-1}, 343 K, 98% RH), metal phosphates such as $(NH_4)_2Al_4(PO_4)_4(HPO_4)\cdot H_2O$ (10^{-4} S cm^{-1}, 343 K, 99% RH) and metal phosphites, like $(NH_4)_{0.59}(H_3O)_{1.41}Mn_5(HPO_3)_6$ (10^{-4} S cm^{-1}, 328 K, 98% RH).[47–55] By linearly fitting the relationship between $\ln(\sigma T)$ and $1000/T$, the activation energy of proton transport is estimated to be 1.50 eV at 98% RH between 303 K and 323 K while the E_a is 0.26 eV between 328 K to 348 K (Fig. 5d). Therefore, the above results suggest that the vehicle mechanism and the Grotthuss mechanism should exist in the temperature range of 303–348 K according to the value of E_a (vehicle mechanism: $E_a > 0.4$ eV; Grotthuss mechanism: $E_a < 0.4$ eV).[2,56] The proton conduction pathway could be further understood by analyzing the structure of the compound and the E_a value. As shown in Fig. S4,† a 1D H-bonding array can be constructed because of the H-bond interactions between histidine molecules and sulfite groups, which should be active in promoting a Grotthuss type conduction. In the temperature range of 328–348 K, the E_a was measured to be 0.26 eV, which is quite a low value suggesting probably the Grotthuss mechanism. However, the activation energy of compound **1** is higher at low temperatures (303–323

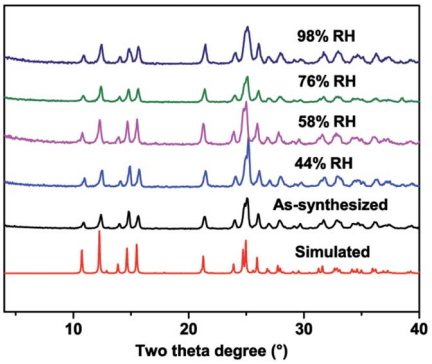

Fig. 6 PXRD patterns of simulated, as-synthesized, and after impedance test under different humidity phases of compound **1**.

K), the E_a is estimated to be 1.50 eV, showing that the proton transport process follows the vehicle mechanism, proton conduction may be due to the diffusion or transfer of crystalline water molecules between layers, which requires a higher activation energy.[2] A similar phenomenon has been reported in a lanthanide carbonate cluster based MOF with the formula $\{[Gd_2(CO_3)(ox)_2(H_2O)_2]\cdot 3H_2O\}_n$.[57]

To further investigate the humidity and temperature stability of compound **1**, we performed a PXRD test on samples after the electrochemical test under different humidity and temperature conditions. As shown in Fig. 6, the structure of compound **1** did not change even after electrochemical testing under conditions of 348 K and 98% RH, indicating that compound **1** has good structural stability, and this property is valuable in practical applications.

TGA analysis

Thermogravimetric analysis carried out in the air at a heating rate of 10 °C min^{-1} up to temperature of 800 °C. The continuous two-step weight loss was observed in the range of 220–673 °C. The total observed weight loss of 71.94 wt% is attributed to the removal of water molecules (calcd 2.91 wt%) and the decomposition of L-histidine (calcd 50.11 wt%) and the sulfur dioxide molecule (calcd 20.67 wt%) in the framework (Fig. S8†).

Photoluminescence spectrum

The photoluminescence spectra of **1** and the histidine molecules were measured in a solid state at room temperature (Fig. S9†). The emission spectrum of $Zn_2(SO_3)_2(C_6N_3O_2H_9)$ showed a peak at 465 nm and excited at a wavelength of 407 nm, red-shifted compared to pure L-histidine. The reason is that the coordination between histidine and zinc ions effectively increases the rigidity of the ligand and reduces the energy loss through non-radiative thermal vibration.[58–61]

Conclusions

In summary, a two-dimensional layered zinc sulfite coordinated by histidine is synthesized under hydrothermal conditions. Notably, an amino acid is firstly introduced into the family of metal sulfites. Proton conductivity investigations on the title compound have been carried out and the proton transmission rate was estimated to be 10^{-3} S cm^{-1} at 348 K and 98% humidity. Additionally, the vehicle and Grotthuss proton conduction mechanisms are realized at 303–323 K and 328–348 K, respectively, which can be attributed to the transfer of crystalline water molecules and the 1D H-bonding array in the framework. Our investigation further exemplifies the possibility of constructing a metal sulfite with biofunctional molecules and exploring a new proton-conducting material in metal sulfite systems. Further work on the syntheses of such metal sulfite analogues for proton conduction is in progress.

Conflicts of interest

There are no conflicts to declare.

Acknowledgements

We thank National Natural Science Foundation of China (No. 21201095, 51663020 and 21301170), Educational Bureau of Liaoning Province for the Fundamental Research of Key Lab (No. L2017LZD002) and the National Science Fund for Distinguished Young Scholars of Guangxi Province (No. 2017JJG150011) for financial support.

References

1 J. A. Hurd, R. Vaidhyanathan, V. Thangadurai, C. I. Ratcliffe, I. L. Moudrakovski and G. K. Shimizu, *Nat. Chem.*, 2009, **1**, 705–710.
2 X. Meng, H.-N. Wang, S.-Y. Song and H.-J. Zhang, *Chem. Soc. Rev.*, 2017, **46**, 464–480.
3 X. Guan, Y. Ma, H. Li, Y. Yusran, M. Xue, Q. Fang, Y. Yan, V. Valtchev and S. Qiu, *J. Am. Chem. Soc.*, 2018, **140**, 4494–4498.
4 M. Inukai, S. Horike, T. Itakura, R. Shinozaki, N. Ogiwara, D. Umeyama, S. S. Nagarkar, Y. Nishiyama, M. Malon, A. Hayashi, T. Ohhara, R. Kiyanagi and S. Kitagawa, *J. Am. Chem. Soc.*, 2016, **138**, 8505–8511.
5 K. M. Mauritz and R. B. Moore, *Chem. Rev.*, 2004, **104**, 4535–4585.
6 G. Alberti and M. Casciola, *Solid State Ionics*, 2001, **145**, 3–16.
7 F. Yang, G. Xu, Y. Dou, B. Wang, H. Zhang, H. Wu, W. Zhou, J.-R. Li and B. Chen, *Nat. Energy*, 2017, **2**, 877–883.
8 M. Sadakiyo, T. Yamada and H. Kitagawa, *ChemPlusChem*, 2016, **81**, 691–701.
9 A. Shigematsu, T. Yamada and H. Kitagawa, *J. Am. Chem. Soc.*, 2011, **133**, 2034–2036.
10 Y. Ye, L. Zhang, Q. Peng, G. Wang, Y. Shen, Z. Li, L. Wang, X. Ma, Q.-H. Chen, Z. Zhang and S. Xiang, *J. Am. Chem. Soc.*, 2015, **137**, 913–918.
11 S. Bureekaew, S. Horike, M. Higuchi, M. Mizuno, T. Kawamura, D. Tanaka, N. Yanai and S. Kitagawa, *Nat. Mater.*, 2009, **8**, 831–836.
12 T. Su, H. Xing, J. Xu, J. Yu and R. Xu, *Inorg. Chem.*, 2011, **50**, 1073–1078.

13 G.-M. Wang, J.-H. Li, X. Zhang, J.-Q. Jiao, Z.-Z. Bao, X.-M. Zhao, W.-W. Jiang, Y.-X. Wang and J.-H. Lin, *Inorg. Chem. Commun.*, 2014, **46**, 295–300.
14 P. Ramaswamy, S. Mandal and S. Natarajan, *Inorg. Chim. Acta*, 2011, **372**, 136–144.
15 K. Wang, Y. Bian, J. Li, D. Xu and Z. Lin, *Inorg. Chem.*, 2016, **55**, 3727–3729.
16 Z.-Z. Xue, J. Pan, J.-H. Li, Z.-H. Wang and G.-M. Wang, *J. Mol. Struct.*, 2017, **1138**, 1–5.
17 S. R. Marri, S. Mahana, D. Topwal and J. N. Behera, *Dalton Trans.*, 2017, **46**, 1105–1111.
18 K. Wang, D. Luo, D. Xu, F. Guo, L. Liu and Z. Lin, *Dalton Trans.*, 2014, **43**, 13476–13479.
19 X. Zhao, C. Mao, X. Bu and P. Feng, *Chem. Mater.*, 2014, **26**, 2492–2495.
20 S. Horike, D. Umeyama, M. Inukai, T. Itakura and S. Kitagawa, *J. Am. Chem. Soc.*, 2012, **134**, 7612–7615.
21 M. Sadakiyo, T. Yamada, K. Honda, H. Matsui and H. Kitagawa, *J. Am. Chem. Soc.*, 2014, **136**, 7701–7707.
22 A. Mallick, T. Kundu and R. Banerjee, *Chem. Commun.*, 2012, **48**, 8829–8831.
23 T. Kundu, S. C. Sahoo and R. Banerjee, *Chem. Commun.*, 2012, **48**, 4998–5000.
24 M. Wei, X. Wang and X. Duan, *Chem.–Eur. J.*, 2013, **19**, 1607–1616.
25 S. S. Nagarkar, S. M. Unni, A. Sharma, S. Kurungot and S. K. Ghosh, *Angew. Chem., Int. Ed.*, 2014, **53**, 2638–2642.
26 G.-L. Zheng, G.-C. Yang, S.-Y. Song, X.-Z. Song and H.-J. Zhang, *CrystEngComm*, 2014, **16**, 64–68.
27 M. Bazaga-Garcia, R. M. P. Colodrero, M. Papadaki, P. Garczarek, J. Zon, P. Olivera-Pastor, E. R. Losilla, L. Leon-Reina, M. A. G. Aranda, D. Choquesillo-Lazarte, K. D. Demadis and A. Cabeza, *J. Am. Chem. Soc.*, 2014, **136**, 5731–5739.
28 G.-G. Cao, J.-D. Liu, T.-T. Zhuang, X.-H. Cai and S.-T. Zheng, *Chem. Commun.*, 2015, **51**, 2048–2051.
29 M. Wang, H.-B. Luo, J. Zhang, S.-X. Liu, C. Xue, Y. Zou and X.-M. Ren, *Dalton Trans.*, 2017, **46**, 7904–7910.
30 H.-R. Zhao, C. Xue, C.-P. Li, K. Zhang, H.-B. Luo, S.-X. Liu and X.-M. Ren, *Inorg. Chem.*, 2016, **55**, 8971–8975.
31 J. Shi, K. Wang, J. Li, H. Zeng, Q. Zhang and Z. Lin, *Dalton Trans.*, 2018, **47**, 654–658.
32 C. Guo, C. Chen, K. Wang, H. Zeng and Z. Lin, *Inorg. Chem. Commun.*, 2017, **85**, 96–99.
33 Y. Yu, J. Zhu, J. Liu, Y. Yan and X. Song, *Dalton Trans.*, 2017, **46**, 9157–9162.
34 B. Manna, B. Anothumakkool, A. V. Desai, P. Samanta, S. Kurungot and S. K. Ghosh, *Inorg. Chem.*, 2015, **54**, 5366–5371.
35 K. Wang, T. Li, H. Zeng, G. Zou, Q. Zhang and Z. Lin, *Inorg. Chem.*, 2018, **57**, 8726–8729.
36 L. Huang, T. Song, Y. Fan, L. Wang, C. Ji, L. Shan and L. Wang, *Microporous Mesoporous Mater.*, 2012, **149**, 95–100.
37 F. Gao, L. Huang, Z. Xiu, Y. Yin, Y. Ma, Y. Bi and Z. Zheng, *CrystEngComm*, 2018, **20**, 5544–5550.
38 G. I. Chilas, N. Lalioti and T. Vaimakis, *Dalton Trans.*, 2010, **39**, 8296–8305.
39 R. K. Tiwari and J. N. Behera, *Dalton Trans.*, 2017, **46**, 5911–5917.
40 R. K. Tiwari, J. Kumar and J. N. Behera, *Chem. Commun.*, 2016, **52**, 1282–1285.
41 G. M. Sheldrick, *SHELXTL-NT, Version 5.1*, Bruker AXS Inc., Madison, WI, 1997.
42 D. T. Cromer and J. T. Waber, *International Tables for X-Ray Crystallography*, Kynoch Press, Birmingham, AL, 1974, vol. 4, Table 2.2A.
43 J. Fan, C. Slebodnick, R. Angel and B. E. Hanson, *Inorg. Chem.*, 2005, **44**, 552–558.
44 L. Chen and X. Bu, *Chem. Mater.*, 2006, **18**, 1857–1860.
45 L. Zhao, J. Li, P. Chen, Z. Dong, J. Yu and R. Xu, *CrystEngComm*, 2008, **10**, 497–501.
46 S. C. Sahoo, T. Kundu and R. Banerjee, *J. Am. Chem. Soc.*, 2011, **133**, 17950–17958.
47 X. Xie, S. Yu, C. Yang, J. Zhang, Z. Li and G. Li, *New J. Chem.*, 2018, **42**, 20197–20204.
48 D. Umeyama, S. Horike, M. Inukai, Y. Hijikata and S. Kitagawa, *Angew. Chem., Int. Ed.*, 2011, **50**, 11706–11709.
49 W. Li, L. X. Xu, D. Luo, H. Wu, J. Tu and M. Yang, *Eur. Polym. J.*, 2007, **43**, 522–528.
50 M. Zhu, Z.-M. Hao, X.-Z. Song, X. Meng, S.-N. Zhao, S.-Y. Song and H.-J. Zhang, *Chem. Commun.*, 2014, **50**, 1912–1914.
51 J. Li, X.-L. Cao, Y.-Y. Wang, S.-R. Zhang, D.-Y. Du, J.-S. Qin, S.-L. Li, Z.-M. Su and Y.-Q. Lan, *Chem.–Eur. J.*, 2016, **22**, 9299–9304.
52 C. Xue, Y. Zou, S.-X. Liu, X.-M. Ren and Z.-F. Tian, *J. Solid State Chem.*, 2018, **258**, 695–701.
53 S. D. Mikhailenko, S. Kaliaguine and E. Ghali, *Microporous Mater.*, 1997, **11**, 37–44.
54 S. Shalini, S. Aggarwal, S. K. Singh, M. Dutt, T. G. Ajithkumar and R. Vaidhyanathan, *Eur. J. Inorg. Chem.*, 2016, **27**, 4382–4386.
55 S. Shalini, V. M. Dhavale, K. M. Eldho, S. Kurungot, T. G. Ajithkumar and R. Vaidhyanathan, *Sci. Rep.*, 2016, **6**, 32489.
56 P. Ramaswamy, N. E. Wong and G. K. H. Shimizu, *Chem. Soc. Rev.*, 2014, **43**, 5913–5932.
57 Q. Tang, Y.-L. Yang, N. Zhang, S.-H. Zhang, F.-S. Tang, J.-Y. Hu, Y.-Z. Zheng and F.-P. Liang, *Inorg. Chem.*, 2018, **57**, 9020–9027.
58 S. Khatua, A. Santra, S. Padmakumar, K. Tomar and S. Konar, *ChemistrySelect*, 2018, **3**, 785–793.
59 M. D. Allendorf, C. A. Bauer, R. K. Bhakta and R. J. Houk, *Chem. Soc. Rev.*, 2009, **38**, 1330–1352.
60 L. Wen, Y. Li, Z. Lu, J. Lin, C. Duan and Q. Meng, *Cryst. Growth Des.*, 2016, **6**, 530–537.
61 W. Feng, Y. Xu, G. Zhou, C. Zhang and X. Zheng, *Inorg. Chem. Commun.*, 2007, **10**, 49–52.